

ASSESSMENT OF THE LANDING CAPABILITIES OF A FLEXIBLE HIGH-ALTITUDE PLATFORM AT LONGITUDINAL AND LATERAL-DIRECTIONAL WIND DISTURBANCES

Yasim J. Hasan[1]

[1]Institute of Flight Systems, German Aerospace Center (DLR), Lilienthalplatz 7, 38108 Braunschweig, Germany, yasim.hasan@dlr.de, +49 531 295 3361

Abstract

So-called high-altitude platforms (HAP) are designed to operate at very high altitudes and are, in principle, capable of staying airborne permanently. Nevertheless, in practice, regular landings remain indispensable due to limited battery cycles and the need for maintenance and repair. Therefore, the safe operation of HAP aircraft during landing under realistic wind conditions must be ensured. However, due to a high aerodynamic efficiency, lightweight structure, extremely low airspeed and a very high susceptibility to wind disturbances, the landing of such aircraft forms a very critical phase and therefore needs thorough investigation. DLR (German Aerospace Center) is currently developing a solar-powered HAP in the context of the program *HAP*. The next step in the project is a comprehensive flight test campaign of the developed aircraft. For the success of the latter, an in-depth understanding of the aircraft's landing capabilities is crucial as well. Therefore, this work deals with landing simulations of the flexible DLR HAP aircraft. In doing so, a large number of landings of the aircraft is simulated under different wind conditions and the aircraft is assessed with respect to its success rate. The test cases comprise constant wind, wind shear and gusts, each from different horizontal directions between 0° and 180° with respect to the runway and encountered at different altitudes. Moreover, light continuous turbulence is superimposed in all cases. The underlying aircraft model includes static and dynamic aeroelastic effects. Furthermore, it features a ground effect model that includes influences in longitudinal and lateral-directional motion, as well as the aeroelastic changes close to ground. The results show that safe landings are possible at most moderate wind conditions. However, crosswind shear and tail gusts before touchdown are found to be critical.

Keywords: High-Altitude Platform, Landing Simulations, Flight Control, Atmospheric Disturbances

1. Introduction

High-altitude platforms (HAP), also known as high-altitude long-endurance (HALE) aircraft, are designed to be operated at high altitudes and for a very long duration, including over-night flight. This makes such vehicles well suitable for typical satellite applications. These include Earth observation missions [1], telecommunications [2] and many others. For this reason, the research on HAP has significantly increased in the last decades [3–8].

Moreover, the use of HAP aircraft for such missions offers some remarkable benefits over the operation of satellites. The latter are always dependent on their orbit. Once launched, their ground track is predetermined and their associated passing times over different Earth locations are fixed. In addition, subsequent modifications of carried equipment is not possible any more. HAP, on the other hand, are more flexible with respect to operation purposes. They can navigate to any location, only constrained by environmental conditions, especially available solar radiation. Furthermore, after having completed a mission, these aircraft can be landed, inspected, equipped with different instruments, relocated and used again for a subsequent mission. The economical and ecological advantages are thus obvious.

Nevertheless, this requires their safe operation during all flight phases. This also includes the landing phase, which is supposedly the bottleneck for HAP aircraft. As HAP aircraft are designed for extremely efficient flight at very high altitudes, they suffer from characteristics that bring significant disadvantages with respect to landing. These are, first, a high aerodynamic efficiency, yielding low achievable stable rates of descent. Second, they have an extremely low weight and third, operate at very slow airspeeds. Fourth, due to the strict weight restrictions, these aircraft are usually designed without air brakes. Fifth, a retractable landing gear would also impose an excess weight penalty. Instead, small non-retractable gears are used. Altogether, these properties lead to a long landing duration and an increased time of flight close to ground, high susceptibility to wind disturbances and a low minimum ground clearance that impedes the continuous use of propellers. After descending below a certain height above ground, a go-around is not possible any more. For these reasons, a thorough investigation of the landing performance of HAP aircraft is indispensable to understand and possibly mitigate landing risks.

The German Aerospace Center (DLR) is currently developing a HAP system within the program *HAP* [9]. The underlying aircraft has a total mass of around 136 kg and was initially designed to perform Earth observation missions in the lower stratosphere that take up to 30 days. The program deals with the fixed-wing HAP aircraft itself, the flight control system [10, 11] and the full operational concept, the ground segment, the flight termination system and two instruments used as payload with a mass of up to 5 kg each. The payload consists of either a high-definition camera [12] or a synthetic aperture radar [13], which can be installed, one at a time, inside the aircraft nose. The program has passed the flight test readiness review and a comprehensive flight test campaign is planned in the next step. It is designed as a series of multiple single flights, in which, besides others, system identification manoeuvres will be performed [14]. Since the flight test campaign requires multiple landings, a thorough understanding of the aircraft's landing capabilities is thus a key for the success of the complete flight test campaign.

For this purpose, this paper deals with the landing of the DLR HAP aircraft at different wind conditions. It performs numerous landings at constant wind, wind shear and gust conditions, each from different horizontal directions between 0° and 180° and encountered at different altitudes with continuous turbulence superimposed. The landings are realised by a control and guidance system for longitudinal and lateral-directional motion. These follow a special landing procedure that was designed for the DLR HAP aircraft [15]. Furthermore, the controller reduces the wind-induced lateral offsets before touchdown. Every landing is then assessed with respect to its success based on a number of predefined conditions.

This paper is structured as follows: section 2 presents the DLR HAP aircraft, as well as the flight dynamics model and flight control system used to perform the landing simulations. Consecutively, section 3 describes the simulation scenario, listing the test points with the different wind conditions and presenting the conditions based on which single cases are assessed as success or failure. Section 4 shows and discusses the overall results and section 5 concludes this paper.

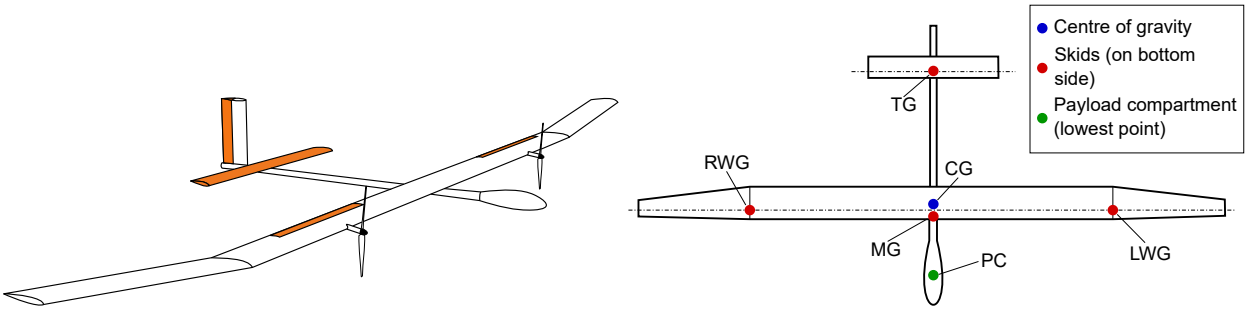
2. The DLR HAP aircraft

This section presents the DLR HAP aircraft, and the flight dynamics model and the flight control system that are used to perform the landing simulations

2.1 The Aircraft

Figure 1 shows a sketch of the HAP aircraft designed and developed by DLR within the last years. It is a flexible fixed-wing aircraft with a wing area of around 36 m^2, a wing span of approximately 27 m and a total mass of around 136 kg. The wing is shaped without sweep and with outer parts with a dihedral angle of 12°. Figure 1a provides a sketch emphasising the aircraft's control surfaces. Inputs are applicable with two oppositely deflected ailerons, a rudder and an movable horizontal tailplane (HTP), denoted as stabilizer in this work. Two electrically-driven propellers with a diameter of 1.7 m are used.

The HAP aircraft has four non-retractable skids. Figure 1b shows the top view of the HAP aircraft and illustrates their positions. The main skid (MG) is located in the aircraft centre line 40 cm ahead of the centre of gravity (CG). Furthermore, wing skids are provided at the left wing kink (LWG) and at



(a) Conceptual sketch with control surfaces highlighted in orange [16]

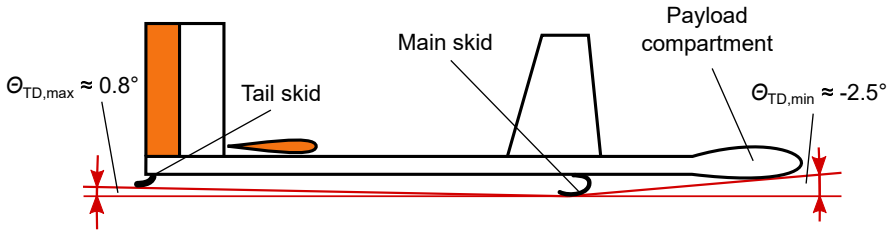
(b) Top view with skid positions, centre of gravity and payload compartment, based on [15]

Figure 1 – DLR HAP aircraft

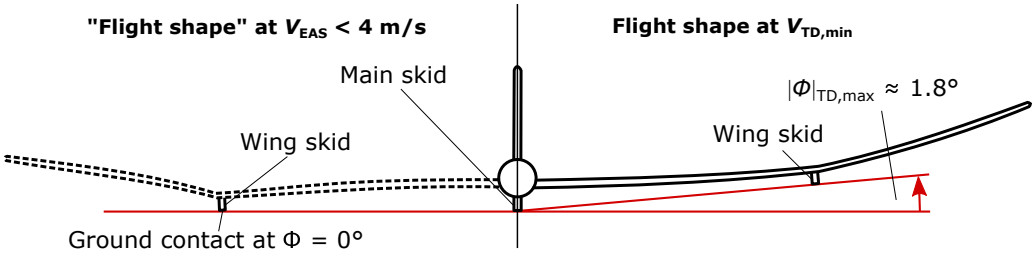
the right wing kink (RWG). Finally, a small tail skid (TG) is installed below the HTP quarter-chord line. The figure also depicts the lowest part of the payload compartment (PC) located inside the aircraft nose. Here, the highly sensitive instruments are stored. Therefore, it must not make ground contact to prevent damage to the payload.

Figure 2 provides more information about the skids. The main skid is supposed to touch down first. Together with with the payload-compartment-related condition, this yields a maximum allowable pitch band, defined by $\Theta_{\mathrm{TD,min}}$ and $\Theta_{\mathrm{TD,max}}$ (Figure 2a). In addition, this yields a maximum allowable bank angle $|\Phi|_{\mathrm{TD,max}}$ (Figure 2b).

It must be noted that these values form a general guidance to the controller or pilot on how the aircraft is supposed to land. By touching down with the main skid first, followed by a controlled touchdown of the tail skid and the wing skids as soon as the airspeed decreases on ground, a higher degree of control over the tail and wing skid touchdown is possible. However, these condition are not used to evaluate the success of a landing. Instead, the maximum occurring forces at each skid are tracked directly.



(a) Side view of HAP aircraft with skids and pitch angles that define the target touchdown band, based on [15]



(b) Front view of HAP aircraft at different flight shapes with skids and allowable bank angle at touchdown

Figure 2 – Side and front view of DLR HAP aircraft showing target touchdown angle band

Furthermore, the wings bend downwards as soon as the airspeed decreases due to the lack of dynamic pressure and thus aerodynamic forces. This allows all skids to have ground contact simultaneously below an airspeed of 4 m/s (Figure 2b, left side) at a bank angle of 0°. At the minimum touchdown speed $V_{\mathrm{TD,min}}$, the wing skids would touch down at bank angles with an absolute value higher than 1.8° (Figure 2b, right side).

2.2 Flight Dynamics Model Formulation for Flexible Aircraft

The flight dynamics model used within this work has, in most parts, already been described in previous works. Therefore, only a brief overview is provided here. For detailed information the reader is referred to the respective works mentioned below. The rigid-body equations of motion are given by

$$\begin{aligned}\dot{\vec{V}}_K &= -\vec{\Omega}_K \times \vec{V}_K + \frac{1}{m}\left(\vec{F}_{Prop} + \vec{F}_{Grav} + \vec{F}_{Aero,RB} + \vec{F}_{Aero,Flex} + \vec{F}_{Skids}\right), \\ \dot{\vec{\Omega}}_K &= \underline{\underline{I}}^{-1}\left[-\vec{\Omega}_K \times \left(\underline{\underline{I}}\vec{\Omega}_K\right) + \vec{M}_{Prop} + \vec{M}_{Aero,RB} + \vec{M}_{Aero,Flex} + \vec{M}_{Skids}\right],\end{aligned} \tag{1}$$

where index K denotes the flight-path-related quantities, $\vec{V}$ is the velocity vector, $\vec{\Omega}$ is the vector of rotational rates and m is the aircraft's total mass. The terms $\vec{F}$ and $\vec{M}$ represent the forces and moments, where contributions due to the propellers (index Prop), gravity (index Grav), rigid-body aerodynamics (Aero) and the skids (Skids) are considered. In addition, aerodynamic forces due to flexibility is accounted for. Coupling between rigid-body motion and structural modes is realised as proposed by Waszak and Schmidt [17] via the aerodynamic forces. Therefore, Eq. 1 includes the forces due to the structural modes (denoted "Aero, Flex"). The according structural dynamics are included using the structural normal modes η_i. The associated equations of motion for all modes read

$$\ddot{\eta}_i + 2\,D_i\,\omega_{0,i}\,\dot{\eta}_i + \omega_{0,i}^2\,\eta_i = \frac{Q_i}{m_i}, \tag{2}$$

where D_i is the damping of this mode and $\omega_{0,i}$ is its natural frequency. Here, the generalised forces Q_i in Eq. 2 account for the forces and moments due to rigid-body flight quantities and due to the coupling of the flexible modes. This completes rigid-body-flexibility coupling. The model accounts for aerodynamic influences of the flight shapes, i.e. the steady deformation at a given airspeed in a horizontal $1g$-flight. In doing so, different sets of aerodynamic parameters are given for different airspeeds. For intermediate airspeeds, interpolation is performed [16]. The structural modes' deflection in Eq. 2 is defined relative to the current flight shape. This way, airspeed excursions affect both the structural modes (through the generalised forces Q_i) and the flight shapes (through interpolation). To cope with this issue, a frequency blending is used with a cutoff frequency of 0.5 Hz. Here, the low-frequency portion of the airspeed is used to apply flight-shape changes and the high-frequency portion is used to excite the modes [14, 18].

All aerodynamic forces that account for rigid-body, flexibility and their coupling are modelled using a derivative approach [14, 16, 18]. Aerodynamic forces are considered separately at main wing, HTP and vertical tailplane (VTP). This allows to account for lag effects of downwash and wind disturbances. Furthermore, stall is modelled at the main wing and VTP [19]. The skids are modelled using standard-linear solids with visco-elastic properties [15, 20].

Compared to earlier works [15, 20] on the landing of the DLR HAP aircraft, the ground effect model was updated and broadly extended. It now considers steady and quasi-steady ground effect influences for longitudinal and lateral-directional motion, as well as the changes of the aircraft's aeroelastic properties when flying close to ground. In addition, influences due to a non-zero flight path angle close to ground are considered, as such a flight condition is an unsteady-aerodynamics case due to the constant change of circulation when approaching the ground or vice versa [21]. This way, the complete flight mechanical changes during flight in ground proximity is reproduced. This is crucial for the HAP aircraft as landing lasts clearly longer than for conventional aircraft. Consequently, flight close to ground cannot be considered as a short transition phase any more as it is the case for more conventional aircraft. This ground effect model accounts for a multitude of parameters, including height above ground, angle of attack, angle of sideslip, pitch angle, bank angle, flight path angle, all rotational rates and all structural-mode deflections and rates. It was obtained by using an unsteady panel method that was particularly developed for flight in ground effect and by identifying a surrogate derivative-based model from it. The full model as well as the approach to obtain it, will be published separately in the future.

2.3 Landing Controller and Guidance

A high number of simulations are performed to assess the DLR HAP aircraft's landing capabilities at the afore-defined different wind conditions, along with random variations of the encounter parameters, respectively the turbulence seed. For this reason, a landing controller and outer guidance modules are used to realise these landings instead of performing pilot-in-the-loop studies. However, landings of the HAP should also be feasible in remotely piloted flight. Therefore, the controllers performance is not supposed to exceed typical piloting capabilities. Consequently, the gains of the implemented controllers were manually tuned and rely on relatively simple inputs with rather low frequency. An earlier work has shown that pilots are indeed capable of landing the aircraft remotely in a similar manner [20].

It must be noted here that the controllers described in this section are only used to enable landings in this work. For the operation of the aircraft within the program *HAP*, different controllers are used [10, 11]. For flight testing, no landing controller is intended. Instead, landings will be performed remotely by pilots, preferably in the augmented mode, which is a rate-command, attitude-hold controller.

Figure 3 shows a simplified sketch of the flight control system used in this work. The outer control loop of the longitudinal controller is based on the well known philosophy of the total-energy control system (TECS) [22–24], while the inner loop consists of a PID-pitch-controller [15]. Longitudinal guidance is realised by an altitude- and airspeed-dependent input generator module. In doing so, the module realises a landing that follows a specific landing procedure that is tailored to cope with the HAP aircraft's particularities. Its main purpose is to provide an additional decision altitude at which the aircraft is stabilised before shutting off the engines and setting the propellers parallel to the wing leading edge (called "to retract the propellers" henceforth for the sake of simplicity). Here, the desired pitch angle at touchdown is established and a final decision about whether to perform a go-around or to commit to land is made based on the current wind conditions. In addition, this procedure allows to subdivide different pilot tasks. Within the simulations performed in this work, wind perturbations are either encountered at higher altitudes (constant wind, first constant part of wind shear) or as soon as the propellers have already been retracted (second constant part of wind shear, gust). Therefore, this procedure is only of minor importance here. More information about this procedure can be found in [15, 20].

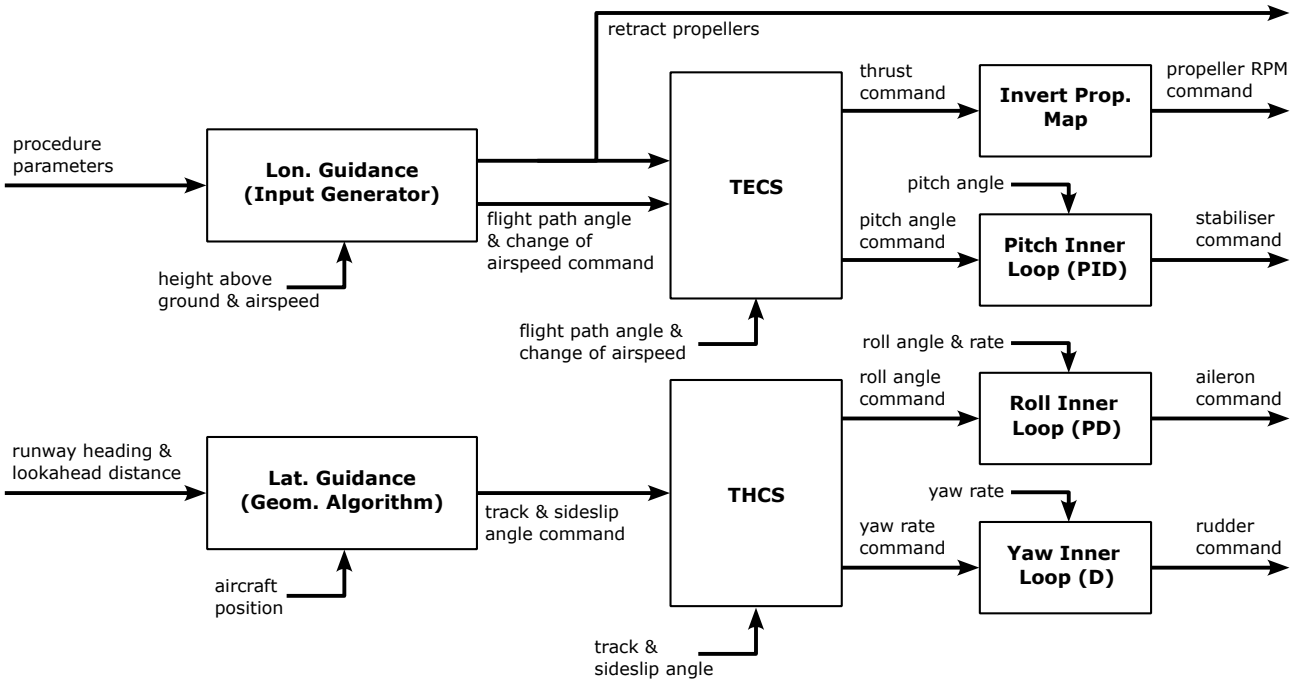


Figure 3 – Simplified sketch of flight control system used for landing simulations

The lateral-directional controller consists of an outer loop that is based on the principle of the total-heading control system (THCS). However, the original concept basically uses sideslip and heading

angle as measurement variables. The DLR HAP aircraft is sluggish and hard to control in the yaw axis, especially at low airspeeds. Therefore, to reduce pilot workload during landing and to counteract lateral drift until touchdown, a decrab maneuver is not foreseen. For this reason, the aircraft is supposed to touch down with a crab angle in case of a crosswind landing. The use of skids as landing gear allows this to a certain extent. Therefore, it is more convenient to use the track angle instead of the heading angle as measurement variable. Accordingly, the THCS variant as proposed by [25] is used. The lateral-directional inner loop consists of a PD-controller for roll and a yaw rate controller. Lateral-directional guidance aims to reduce the lateral offset to the runway centre line and to align the aircraft's track, rather than its heading, with it. In doing so, lateral-directional control inputs need to be limited to cope with loads restrictions. The according guidance module is based on a geometric algorithm that uses a lookahead distance of 200 m on the runway centre line and aims to intercept it. This allows for a smooth transition of the aircraft track with the runway. More information about the according principle can be found in [26].

3. Simulation Scenario

This section outlines the simulation scenario. It first presents the test points that are performed and describes the different wind cases. Second, it lists landing success conditions that are used to assess the landings and to obtain an overall success rate.

3.1 Test Points

The use of HAP aircraft on a regular basis requires that it can be reliably landed at moderate but realistic wind conditions of different type. For this reason, multiple wind types are applied within the simulations performed in this work. Figure 4 sketches the trends of all applied wind types. These are:

- Constant wind with a magnitude of 2 m/s: As shown by Figure 4, the constant wind is applied in the form of a ramp. This trend is chosen deliberately as it is desired that the aircraft encounters the wind at a certain height above ground and does not already start in a trimmed state adapted to the wind. The ramp is chosen to reduce the dynamic aircraft reactions. This modelling approach represents a case in which the aircraft a constant wind field while descending.
- Wind shear with a slope of 1 m/s^2: It is defined in this work with respect to time rather than by a spatial distribution. It is modelled as constant wind of 1 m/s from one direction that changes its direction by 180°, respectively to -1 m/s. Here, the magnitude of the slope is of minor importance. It is chosen such that the dynamic aircraft response is still comparatively small but still enabling a fast change of directions. This condition can be regarded as a worst case wind shear.
- Discrete gusts with a peak velocity of 3 m/s and a wavelength of 50 m: This wavelength is chosen as it has been found to be the most critical. Short wavelengths would indeed cause a larger dynamic aircraft reaction but it would also fade away much faster.

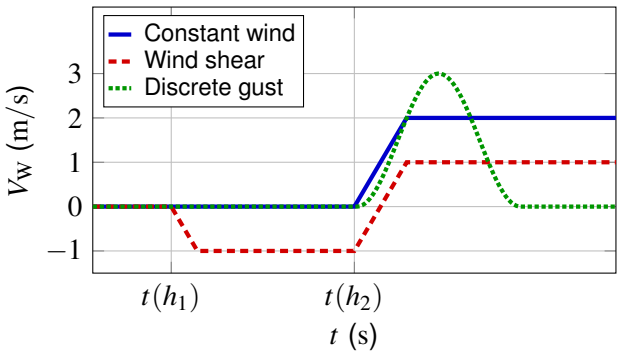


Figure 4 – Wind types used during landing simulations

Each wind type is applied from different directions ranging from 0° to 180° with steps of 45°. For the sake of simplicity, the runway is aligned with the North axis in this scenario. By varying wind between

0° and 180° in steps of 45° both purely longitudinal, purely lateral-directional and combined wind is considered. In all cases, light turbulence according to [20] is applied. Every case is repeated 100 times with randomly varied turbulence seeds to obtain a higher statistical relevance. Table 1 lists all performed test cases.

Table 1 – Landing simulation test cases

Wind type	Turbulence strength	Encounter altitudes h_1	Encounter altitudes h_2	Wind direction	#
Turbulence & constant wind	light		8 m	0°	100
	light		8 m	45°	100
	light		8 m	90°	100
	light		8 m	135°	100
	light		8 m	180°	100
Turbulence & wind shear	light	8 m	2 m – 4 m	0°	100
	light	8 m	2 m – 4 m	45°	100
	light	8 m	2 m – 4 m	90°	100
	light	8 m	2 m – 4 m	135°	100
	light	8 m	2 m – 4 m	180°	100
Turbulence & discrete gust	light		2 m – 4 m	0°	100
	light		2 m – 4 m	45°	100
	light		2 m – 4 m	90°	100
	light		2 m – 4 m	135°	100
	light		2 m – 4 m	180°	100

For every wind type, different altitudes of encounter are used. As shown, constant wind as well as the first part of the wind shear are always encountered at a height above ground of 8 m. This ensures that the aircraft has enough time to counteract the wind and to stabilise at an associated flight condition. The encounter altitude of the change of direction of the wind shear, as well as the gust are varied randomly, again with a uniform distribution, between 2 m and 4 m. This assures that the respective disturbances are encountered after the propellers have been retracted such that a go-around is not possible any more and the aircraft, instead, needs to land. This altitude is varied as neither of the variation limits (2 m or 4 m) necessarily forms a worst case. In addition, this allows, if applicable, to analyse the influence of the encounter altitude.

3.2 Landing Success Conditions

Since a high number of landings are performed, numerical conditions are required, that allow to assess the success of each landing without a manual review of the results. The allowed band for pitch and roll at touchdown and the order with which the skids are supposed to touch down presented in subsection 2.1 only form soft requirements and provide a general guidance for the pilot, respectively the controller, on how to land the aircraft. For an assessment about success or failure, different requirements are needed.

For this purpose, the forces that apply at the different skids are monitored directly and the maximum occurring values are used. As the HAP aircraft has an extremely delicate structure, none of the skids can carry more than the full aircraft weight at any time. In addition, the forces at tail and wing skids are additionally limited due to bending loads. The requirements are defined as follows:

- Maximum main skid force: $F_{\mathrm{MG,max}}/(mg) \overset{!}{\leq} 1.0$.
- Maximum wing skid forces: $F_{\mathrm{LWG,max}}/(mg) \overset{!}{\leq} 0.5$ & $F_{\mathrm{RWG,max}}/(mg) \overset{!}{\leq} 0.5$.
- Maximum tail skid force: $F_{\mathrm{TG,max}}/(mg) \overset{!}{\leq} 0.3$.
- Maximum force at payload compartment: $F_{\mathrm{PC,max}}/(mg) \overset{!}{=} 0.0$.

- Lateral offset at touchdown: $|\Delta y_{\mathrm{RWY}}| \overset{!}{\leq} 7\,\mathrm{m}$.

These requirements depend strongly on the aircraft's structural properties and skid parameters and are specifically tailored to the DLR HAP. Moreover, the last requirement that limits the allowable lateral offset during touchdown depends solely on the runway geometry. In this case, a landing on the runway of airport EDBC, namely Magdeburg-Cochstedt, where the flight test campaign within *HAP* is planned, is used as a reference. Accounting for its width of approximately 45 m and additionally providing a safety margin of 2 m yields approximately 7 m of allowable offset. Due to its length of 2500 m, no maximum length is formulated as a requirement.

4. Results

This section presents the results obtained within the landing simulation series. It is divided into two parts. The first part shows exemplary time histories of one complete landing. The second part presents the distributions of key parameters taking into account all performed landings.

4.1 Exemplary Time Histories of One Landing

Here, a single landing case is presented in order to provide a profound understanding of landings of the HAP aircraft. In addition, this serves to illustrate the landing procedure tailored for the HAP aircraft. Indeed, it is of rather minor importance for the landing results presented in this section because the dynamic wind perturbations are applied after the propellers are retracted. Nevertheless, it is described here since it aims to increase landing safety especially at adverse wind conditions. Figure 5 shows a landing at wind shear conditions with a final wind direction of 135° with respect to the runway, which is assumed to be aligned with the North axis. Hence, the perturbations apply both to longitudinal and lateral-directional motion. In addition, light turbulence is superimposed. The shown landing represents one case of the full landing simulation series.

In the left column, Figure 5 shows time histories from top to down for height above ground h, true airspeed V_{TAS}, active phase of the longitudinal landing guidance "Phase", angle of attack α, sideslip angle β, bank angle Φ, pitch angle Θ, heading angle Ψ, number of revolutions of the propeller N_{Prop}, combined angle of oppositely deflected ailerons $\hat{\xi}$, stabiliser deflection i_{HTP} and rudder deflection ζ. The right column provides the body-fixed wind components in all three axis $u_{\mathrm{W_b}}$, $v_{\mathrm{W_b}}$, $w_{\mathrm{W_b}}$, the lateral aircraft offset to the runway Δy_{RWY}, the first three structural modes with lowest frequency η_1, η_2 and η_3, and the normalised normal forces at the left wing skid $F_{\mathrm{LWG},z}/m$, right wing skid $F_{\mathrm{RWG},z}/m$, main skid $F_{\mathrm{MG},z}/m$, tail skid $F_{\mathrm{TG},z}/m$ and payload compartment $F_{\mathrm{PC},z}/m$. The first structural mode η_1 represents the first wing bending. For the HAP configuration used in this work, the second mode η_2 is an asymmetric wing bending with fuselage torsion and the third mode η_3 is an asymmetric wing bending with lateral fuselage bending [18]. Please note that the aeroelastic model has been updated in the meantime [27]: a ground vibration test has been performed and the structural properties have slightly changed. As a consequence η_2 and η_3 have changed. However, these changes are expected to have no significant influence on the landing dynamics.

The simulation starts at the obstacle altitude h of around 15 m and the aircraft descends towards the decision height h_{Target}, which is set in this work to 5 m. Upon reaching the encounter altitude h_1 of 8 m (cf. Table 1), constant wind applies with a direction of 315°, which is the opposite direction of the final 135° (at approximately 22 s). This wind is encountered as a combination of tail and right crosswind. As a consequence, the respective wind components $u_{\mathrm{W_b}}$ and $v_{\mathrm{W_b}}$ increase in magnitude. The lateral controller reacts with right rudder ζ and aileron $\hat{\zeta}$ input to counteract the resulting sideslip angle β. As a result, a right crab angle is set up. At this point, it must be noted that the controller is tuned to apply very small lateral inputs, as proverse rudder and sideslip form a very critical load case.

While further descending, the lateral offset Δy_{RWY} slightly increases. As soon as the aircraft reaches the decision height h_{Target}, phase 2 is initiated, whereupon the aircraft captures and maintains this altitude. Afterwards, it slightly decelerates (cf. V_{TAS}) until the target pitch angle is reached. This angle is chosen such that it is well inside the allowable pitch band at touchdown (cf. Figure 2a) but closer to the less critical limit of $\Theta_{\mathrm{TD,max}}$. After maintaining this pitch angle for 3 seconds, phase 3 is initiated. In a remotely piloted flight, this would represent that the pilot assesses the current wind conditions as

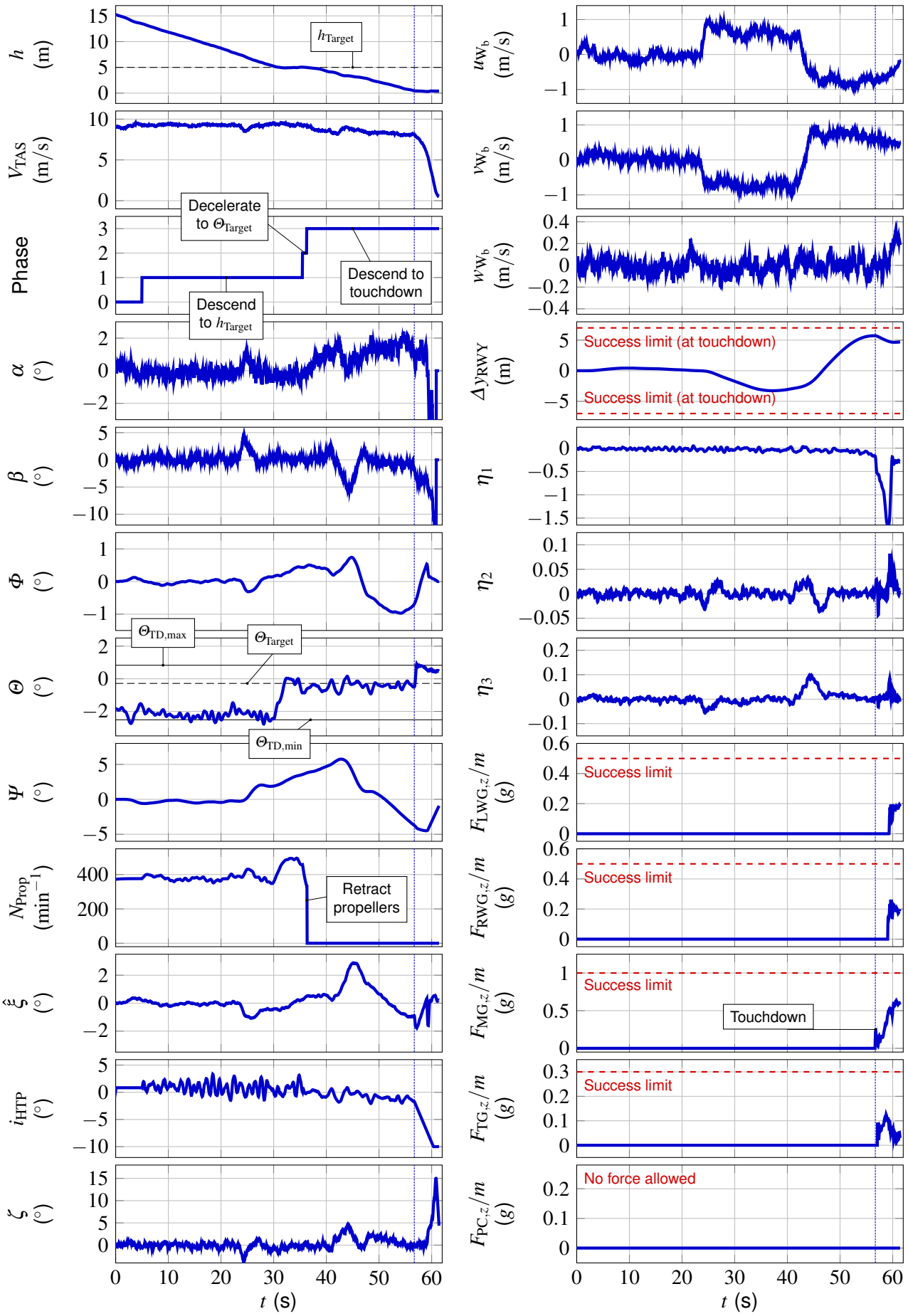


Figure 5 – Time histories of a landing simulation at wind shear with a final direction of 135° (wind from rear right changes to from front left)

acceptable and commits to land the aircraft. Thereupon, the propellers are retracted and the aircraft descends towards the ground (at around 37 s).
As soon as the randomly varied second encounter altitude h_2 (cf. Table 1) is reached, i.e. in this case at approximately 3.5 m (41 s), the wind changes its direction and is henceforth encountered from front left, which again goes along with a reaction of the flight controller commanding the aircraft to turn towards the wind. However, the aircraft initially has a flight condition to counteract wind from the opposite side. As a result from the change of wind direction, it sets up lateral offset Δy_{RWY} to the opposite side quite fast. Attempting to reduce the lateral offset again it turns towards the runway until it ultimately touches down at approximately $56\,s$, which is represented in all plots by a vertical bar. At this point, it must be noted that the aircraft is not supposed to establish a wings-level flight again before touchdown. This is due to the fact that it is very sluggish and levelling the wings would take quite some time. Hence, this time is expected to be used rather to reduce lateral offset. The associated bank angles are small anyway, wherefore the risk of a wing skid touching down first is still low.
As desired, the main skid touches down first ($F_{\mathrm{MG},z}/m$), followed by the tail skid (non-zero values $F_{\mathrm{TG},z}/m$ and $\Theta_{\mathrm{TD,max}}$ reached). This is also accompanied by a small downstroke of the wings (represented by a negative peak of η_1) In the following, the true airspeed V_{TAS} decreases. The associated loss of dynamic pressure causes the flexible dihedral to decrease, which leads to a ground contact of the right wing skid ($F_{\mathrm{RWG},z}/m$), followed by the left wing skid ($F_{\mathrm{LWG},z}/m$). The maximum forces of at the right skid are higher than at the left side. This is in line with the left crab angle with which the aircraft touched down due to the left wind component. This is indicated by the negative heading angle Ψ. Accordingly, a lateral skid-friction component occurs right after touchdown that leads to a small right rolling motion further pushing the right wing skid to the ground. This causes the higher forces at this side. While the aircraft comes to a standstill, the stick is slightly pulled (decrease of i_{HTP}) to ensure that the payload compartment does not make ground contact. This is implemented in the form of an open-loop command that starts after the first ground contact. The payload compartment indeed does not make ground contact, which is shown by the absence of non-zero values of $F_{\mathrm{PC},z}/m$. It is noteworthy that the landing shock at the main skid leads to much smaller values of $F_{\mathrm{MG},z}/m$ than in standstill conditions in which the skid is just carrying a part of the aircraft weight. This is due to the small vertical velocities at touchdown in such a nominal and successful landing case. This shows that a flare is not required to reduce landing shocks for HAP aircraft, as opposed to conventional passenger aircraft.

4.2 Resulting Distributions

Next, the resulting distributions that take into account all simulated landings are presented. For this purpose, Figure 6 shows the overall success rate. It is obtained by evaluating every landing with respect to the success conditions defined in subsection 3.2. As shown, with values of 99 % – 100 % the success rate is good for most test points. However, it is apparent that the crosswind shear forms a critical landing case leading to a failure rate of more than 50 %. The tailwind gust leads to a failure rate of 85 %. In the following, the landing results will be investigated in more detail.
Figure 7 shows the distributions of the maximum forces that occurred during the landings at every skid. Figure 7a shows the normalised maximum skid forces, Figure 7b shows the forces at the tail skids and Figure 7c shows them for the left (top) and right (bottom) wing skids. In addition, the afore-defined success limits are displayed. It can be seen that the forces are well below the limiting conditions in the great majority of cases. Dynamic tailwind conditions are the most critical with respect to skid forces. The tailwind shear leads to increased maximum tail skid forces that are, however, still below the limits. The tailwind gust leads to strongly increased tail skid forces that, in some cases even exceed the limit. In addition, it causes larger maximum main skid forces in some cases. Nevertheless, in the majority of cases, it yields forces that are comparable in size to all other landing cases. This remarkable result will be discussed in more detail later.
Another noteworthy case is the constant crosswind, i.e. with 90°. As shown, it leads to clearly increased maximum forces at the right wing skid. This is due to the fact the the aircraft lands with a left crab angle in these cases, wherefore the lateral skid friction force creates a right rolling moment that

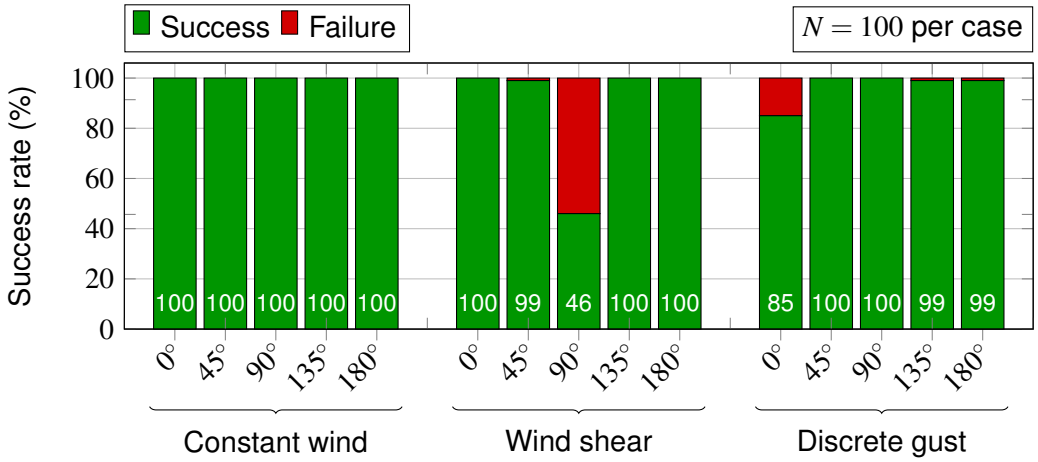
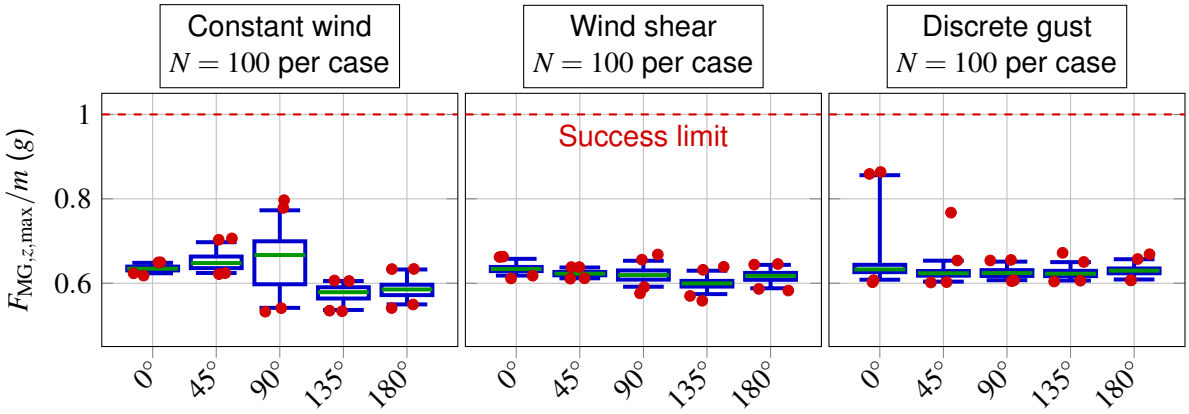


Figure 6 – Success rates for all landing cases

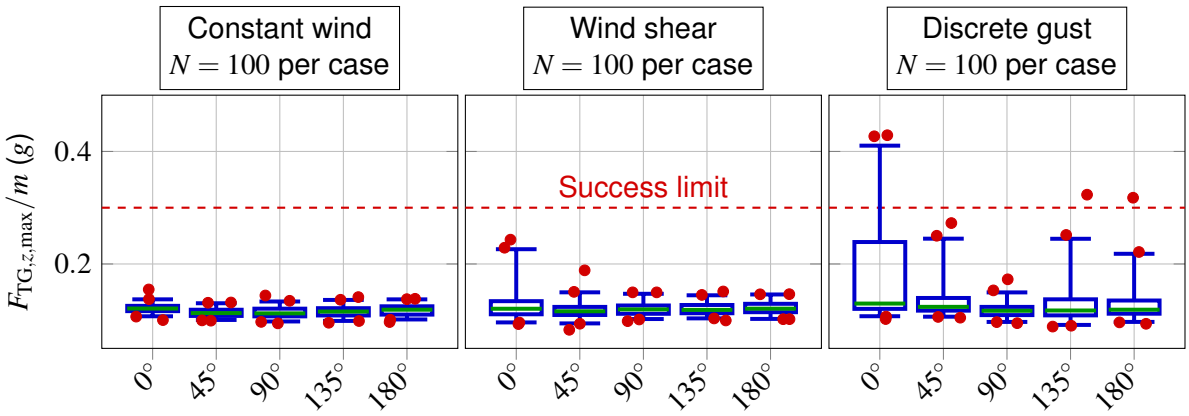
causes a higher skid load on this side. For combined lateral and longitudinal constant wind, i.e. with 45° or 135°, this behaviour is identical but the effect is smaller since the lateral component is smaller likewise. The wind shear shows the same characteristics but the forces are smaller, which is well in line with the fact that a reduced wind magnitude of 1 m/s was applied in these cases. The induced rolling moment after touchdown in the constant-crosswind case also leads to a delayed ground contact of the left wing skid. For this reason, the main skid bears a higher force compared to a nominal landing. In addition, the higher right wing skid force induces a stronger left rolling moment afterwards. In some cases, this can also lead to increased forces at the left skid. In sum, the variation at the left skid is higher compared to different landing cases.
Figure 8 shows the distribution of maximum forces at the payload compartment. As already stated, no ground contact is allowed here. This signifies that zero maximum forces are required. As shown, only the tail gust leads to a touchdown of the payload compartment in rare cases. This behaviour will be discussed in more detail later in this section.
Figure 9 shows the box plots for the lateral offset at the moment of touchdown along with the acceptable limit of 7 m. Here, it becomes apparent that this condition is the sole driver for the high failure rate of the crosswind shear condition. Its median value already exceeds the success limit.
This case is particularly critical because the aircraft is configured to counteract wind from the opposite side before the latter changes its direction. As a result, a strong offset is set up in a short time. It is noteworthy that the wind shear in the direction of 135° leads to higher offsets with smaller variations compared to the case with 45°. In the latter case, the addition tailwind component leads to a clearly faster touchdown with a stronger dependency on the encouner altitude h_2. As a consequence, the aircraft touches down before higher offsets are established. In the case of 135°, the additional headwind component delays touchdown, which causes a higher offset in combination with the additional crosswind component.
In the following, three cases will be investigated in more detail to reveal the main dependencies and to analyse the influences of the encounter altitudes. These are

- crosswind shear,
- crosswind gust and
- tailwind gust.

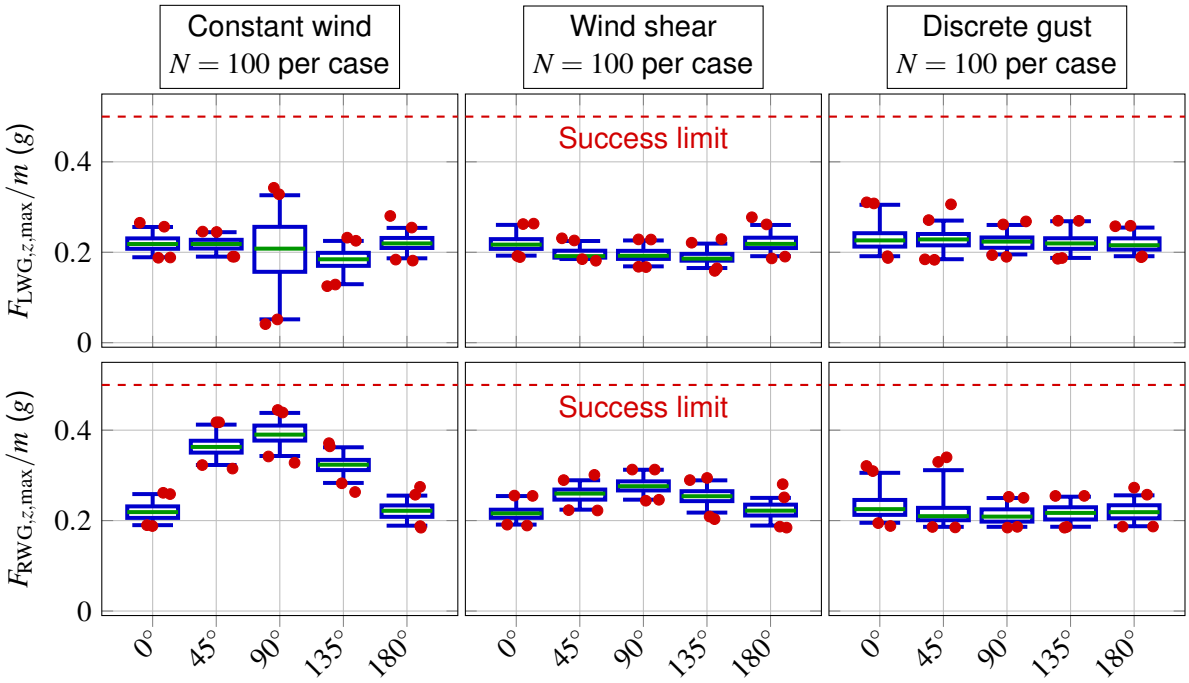
Figure 10 shows a cross plot of the lateral offset over the encounter altitude h_2 for all landings with crosswind shear. Here, the lateral offset decreases with h_2. At an altitude of 4 m the offset is largest. Even though not investigated here, the trend suggests that at higher altitudes the offset would decrease again. In other words, for encounters below 4 m, the aircraft is not able to reduce the resulting offset. Instead, a lower encounter altitude is favourable as the smaller remaining time until touchdown prevents the setup of higher offsets.



(a) Maximum main skid forces



(b) Maximum tail skid forces



(c) Maximum forces at left (upper row) and right (lower row) wing skids

Figure 7 – Distribution of maximum forces at main skid, tail skid and wing skids for all landing cases

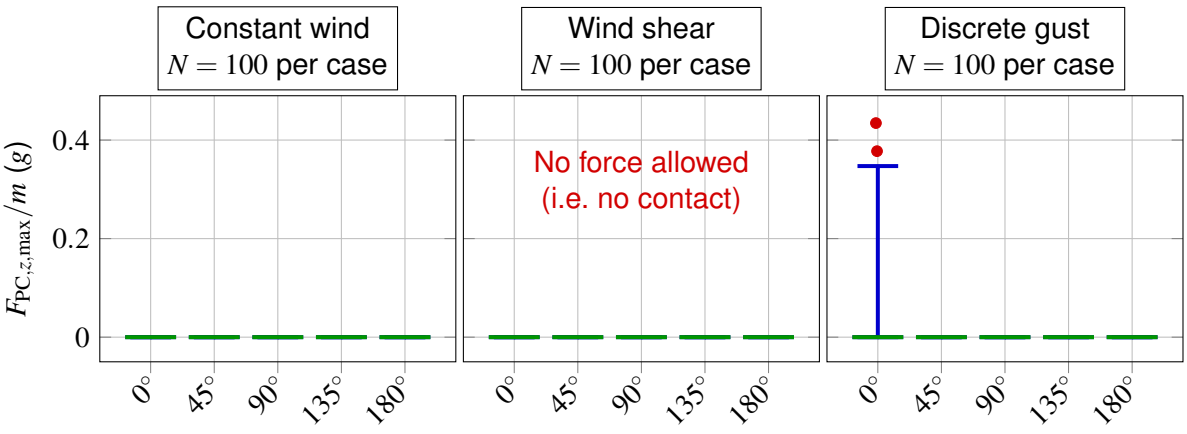


Figure 8 – Distribution of maximum forces at payload compartment for all landing cases

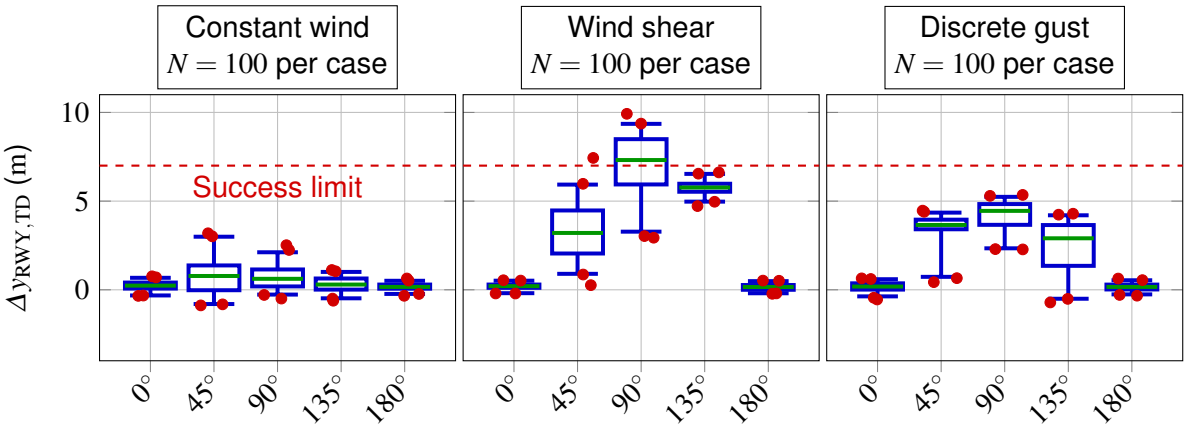


Figure 9 – Distribution of lateral offsets at touchdown for all landing cases

Next, the crosswind gust is regarded. For this purpose, Figure 11 shows three cross plots. These are the lateral offset over encounter altitude (Figure 11a), a measure for the crab angle at the moment of touchdown over encounter altitude (Figure 11b) and touchdown bank angle over touchdown crab angle (Figure 11c).

It was already shown before that the crosswind gust is neither critical with respect to the lateral offset nor the maximum skid forces. As illustrated by Figure 11a, the lateral offset has a reversed dependency on the encounter altitude compared to the crosswind shear. Here, a lower encounter leads to an increased offset. The reason lies in the response of the aircraft to crosswind gusts. As soon as the gust hits the aircraft, it turns into the gust direction due to its weathercock stability, setting up an additional heading angle. This behaviour is augmented by the controller. This reduces the lateral drift. In addition, as soon as the gust decreases again, the aircraft starts to reduce the lateral offset since it is still headed towards the direction of the gust. For smaller encounter altitudes, the aircraft touches down before it can reduce more offset. Nevertheless, due to its short length, the overall lateral drift is small compared to the wind shear, even in this case. However, this also signifies that the aircraft touches down in an unstable flight condition.

Against this background, it is astonishing that the resulting forces at the left and right wind skids are comparatively low (cf. Figure 7c). Indeed, as shown by Figure 11b, the crab angle with which the aircraft touches down is very high, especially at low encounter altitudes. In case of constant crosswind, this angle was the main driver for increased wing-skid forces but this is not the case for the crosswind gust. Figure 11c provides the physical justification. As shown, in cases in which the aircraft touches down with high crab angles, this is always accompanied with higher negative bank angles. A negative bank angle increases the tendency of the left wing skid to touch down before the right skid. In some rare cases, it even touches down before the main skid (for bank angles below -1.8°). In sum, both effects thus balance each other and the resulting wing forces are moderate.

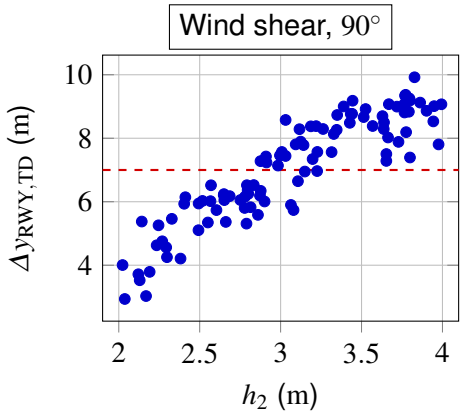
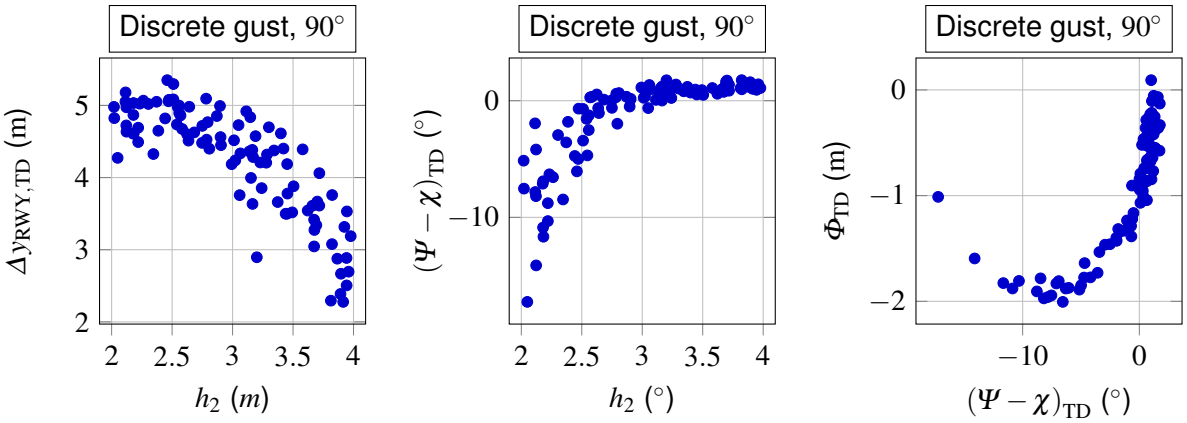


Figure 10 – Lateral offset to runway center line at touchdown over encounter altitude for crosswind-shear landings, full ground effect model



(a) Lateral offset to runway at touchdown over encounter altitude

(b) Crab angle at touchdown over encounter altitude

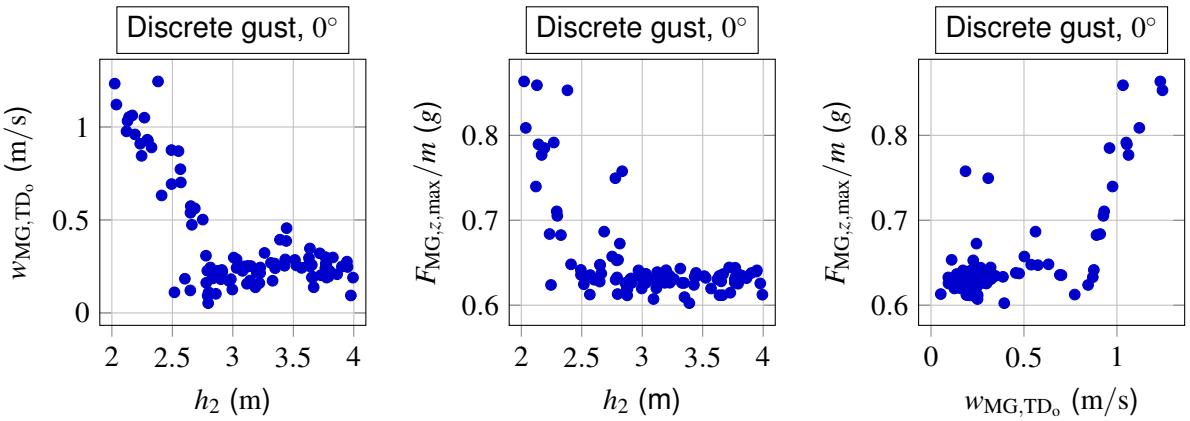
(c) Bank angle at touchdown over crab angle at touchdown

Figure 11 – Cross plots for crosswind-gust landings, full ground effect model

Finally, a closer look is taken at the tailwind gust. This wind case leads to stronger variations of the maximum forces at main skid and tail skid. In addition, with 15 % its failure rate is comparatively high. Both the tail-skid-force limit and payload-compartment ground contact are drivers for the rather high failure rate. Figure 12 shows different cross plots for this wind condition.

Figure 12a depicts the vertical inertial velocity $w_{\mathrm{MG,TD_o}}$ of the main skid at touchdown over the encounter altitude. It can be seen that for encounters below approximately 2.7 m, the vertical velocity is strongly increased. This indicates that the aircraft touches down in a rather uncontrolled flight condition in these cases, while for higher encounters the aircraft could recover from the gust before touchdown. Nevertheless, as documented by Figure 12b, the according maximum forces increase below an altitude of around 2.4 m in most cases, which is smaller than the afore-mentioned 2.7 m. Figure 12c clarifies this mismatch. As shown, a distinct dependency of the maximum forces on the vertical touchdown velocity only exists for larger velocities, i.e. starting at around 0.8 m/s. Only in these cases is the landing shock the main driver for the maximum force. Here, the latter increases with increasing vertical velocity. For smaller vertical velocities at touchdown, on the other hand, the static skid forces due to carrying the aircraft weight at standstill is still higher, wherefore the strength of the landing shock has no influence on the maximum force.

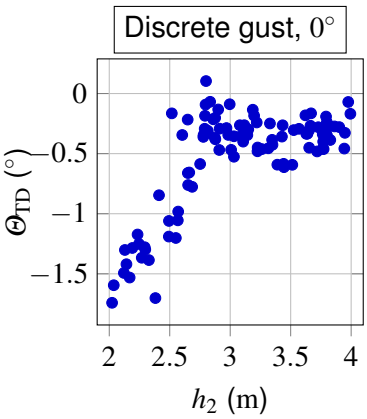
Figure 12d shows the pitch angle at touchdown over the encounter altitude. As a result from a tailwind gust encounter, the aircraft initially pitches down. Therefore, the aircraft touches down with a decreased pitch angle if the gust hits it below the above-mentioned 2.7 m. This is consistent with the above-made conclusion, that the aircraft cannot recover from the gust encounter before touchdown



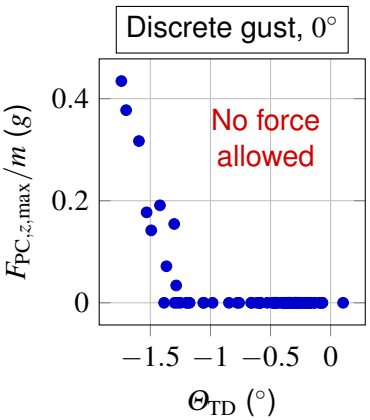
(a) Main-skid vertical velocity at touchdown over encounter altitude

(b) Maximum forces at main skid over encounter altitude

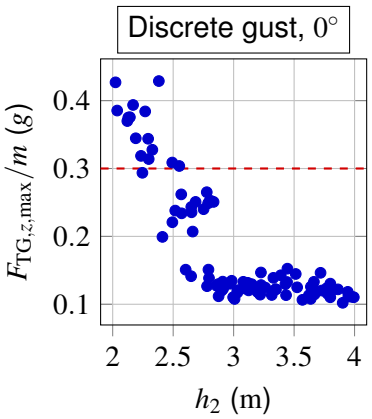
(c) Maximum forces over vertical velocity at touchdown at main skid



(d) Pitch angle at touchdown over encounter altitude



(e) Maximum forces at payload compartment over touchdown-pitch angle



(f) Maximum forces at tail skid over encounter altitude

Figure 12 – Cross plots for tailwind-gust landings, full ground effect model

if it is encountered at this altitude or lower. In the worst case, the associated pitch angle is at around −1.7°. This angle is still higher than the minimum allowable angle from geometrical relations that is driven by a payload-compartment ground contact (cf. Figure 2a). However, as shown by Figure 12e, this does not guarantee that the payload compartment makes no ground contact. Instead, due to the dynamic processes right after touchdown, the payload compartment touches down for all landings with a touchdown pitch angle of around −1.3° or smaller. Finally, Figure 12f shows the distribution of maximum tail skid forces over encounter altitude h_2. It resembles Figure 12a. Hence, if the gust is encountered below 2.7 m, in other words if the aircraft does not have enough time to recover from the gust, the associated maximum forces increases. Here, this even leads to a high probability of a failure case.

Finally, Figure 13 shows box plots for the distributions of landing distances for constant wind with a magnitude of 2 m/s in different directions. These box plots illustrate the distribution of different quantities, where the green bar represents the median value. 50 % of the values lie inside the blue box with 25 % above and 25 % below the median. The outer lines with horizontal bars at their end represent the whiskers that each contain 23 % of the data. The remaining 4 % of data are directly plotted with red dots in the form of outliers. For the present analyses, 100 simulations have been performed. Consequently, two outliers are existent above and two below the whiskers.

As shown, the landing distances increase for wind conditions with tailwind components. This is expectable as the ground speed increases in this case, which leads to higher distances. It can be seen that the increase is not proportional to the directions. For example, the landing distances decrease smaller in average for headwind compared to pure crosswind than they increase for tailwind. This

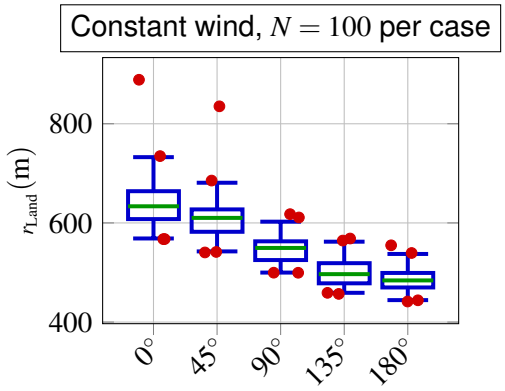


Figure 13 – Landing distance for constant-wind cases

can be attributed to the fact that the aircraft needs some more time to stabilise after first encountering the tailwind than the headwind and, according to the landing procedure, then initiates its final descent later. For the same reason, there are two outliers in the case of directions of 0° and 45°. In these cases, the aircraft retracted the propellers unusually late.
Table 2 summarises the results. In the majority of cases, the landings are successful. Wind shear with crosswind components increase the risk of an excess lateral offset at touchdown. In case of pure crosswind, the success rate is at 46 %. Discrete gusts with longitudinal components, especially tailwind, increase the failure rate. The according failure cases are excess tail skid forces and a ground contact of the payload compartment. At very low encounters both cases most often occur during the same landing.

Table 2 – Summary of results

Wind type	Direction	Representation	Success rate	Failure cases
Turbulence & wind shear	45°	Tail- and crosswind	99 %	Lateral offset
	90°	Crosswind	46 %	Lateral offset
Turbulence & discrete gust	0°	Tailwind	85 %	Maximum tail skid forces Payload compartment ground contact
	135°	Head- and crosswind	99 %	Maximum tail skid forces
	180°	Headwind	99 %	Maximum tail skid forces
All other cases			100 %	

These results show that the DLR HAP aircraft can be landed with a certain degree of reliability. This confirms that the flight test campaign within the program *HAP* can be performed as planned. However, special care must be taken to mitigate the two critical failure cases, being crosswind shear and tailwind gust. The results presented in this paper suggest, for instance, that the wind should be monitored along the runway and not only at a single point to detect changes of the wind direction. In addition, it can be beneficial to reduce the height above ground at which the propellers will finally be retracted.

5. Conclusion and Outlook

This paper analyses the landing capabilities of a high-altitude platform. For this purpose, a high number of simulations are performed using a flight dynamics model of the flexible aircraft with landing skids. It includes a detailed ground effect model that accounts for longitudinal and lateral-directional motion and the interaction of flexible modes with each other and the rigid-body motion. In these simulations, different wind cases are considered. These are constant wind, wind shear and discrete

gusts. At all test points, light turbulence is superimposed and the wind direction is varied. Altogether, 100 simulations are performed for every test point, in which wind parameters are varied at random using a uniform distribution. Longitudinal and lateral-directional guidance and controllers are used to realise the landings, counteract disturbances to a certain extent and to align the aircraft's track with the runway.

Furthermore, a set of landing success requirements are defined, which refer to maximum forces that occurred at the skids and the aircraft's payload compartment as well as to the maximum lateral offset from the runway centre line at touchdown. The results show that landings are possible in all constant-wind cases. In addition, most wind shear conditions and discrete gusts are tolerable. However, two critical wind cases are identified. The first is the crosswind shear that led to a low success rate of only 46 %. If this wind type is encountered in an altitude band between approximately 3 m and 4 m, the associated lateral offset is larger than 7 m. In addition, the tailwind gust is a critical case that led to a success rate of only 85 %. If encountered below 2.4 m, the aircraft touches down in a rather uncontrolled condition. This is associated with the exceedance of tail skid forces or a ground contact of the payload compartment. Main skid forces are also increased in these cases. However, the associated rate of descent with which the aircraft touches down is still low compared to conventional aircraft. Therefore, even in these cases the main skid limit is not yet exceeded.

The landing success conditions that are formulated in this work are specifically tailored to the DLR HAP aircraft and depend especially on the chosen skid parameters. In addition, the allowable offset is chosen for a landing on the airport Magdeburg-Cochstedt (EDBC). Hence, the overall success assessment might change if different requirements apply. However, especially the distributions of key parameters in this paper can be used, e.g. for skid sizing for different HAP aircraft or for choosing appropriate landing fields. For example, the rather high lateral offset at crosswind shear suggests to use a rectangular field for landing instead of a conventional runway.

A logical next step would be to review the most critical wind cases, i.e. crosswind shear and tailwind gusts, in more detail. As an example, it could be investigated to which extent higher control inputs would be applicable to reduce the lateral offset during landing. In this work, control inputs were restricted for the sake of loads limitations. However, the reduction of lateral offset during landing could instead also be used as an additional load case. Moreover, the benefit from changing the target touchdown pitch angle could be assessed. Here, it would be interesting to analyse whether this could reduce the maximum skid forces in case of the tailwind gust. Finally, wind disturbances were only included from a qualitative viewpoint in this work with a fixed magnitude for every wind type. Instead, the magnitudes could be varied. This would yield a wind envelope for landing.

Acknowledgements

The author would like to thank Nicolas Fezans for many fruitful discussions and his invaluable advice on this topic. Moreover, the author would like to acknowledge the colleagues involved in the program *HAP*, particularly those who are part of the flight physics team and thereby contributed in setting up the flight dynamics model used in this work.

Contact Author Email Address

yasim.hasan@dlr.de

Copyright Statement

The authors confirm that they, and/or their company or organization, hold copyright on all of the original material included in this paper. The authors also confirm that they have obtained permission, from the copyright holder of any third party material included in this paper, to publish it as part of their paper. The authors confirm that they give permission, or have obtained permission from the copyright holder of this paper, for the publication and distribution of this paper as part of the ICAS proceedings or as individual off-prints from the proceedings.

References

[1] Runge, H., Rack, W., Ruiz-Leon, A., and Hepperle, M., "A Solar Powered HALE-UAV for Arctic Research," in *1st CEAS European Air and Space Conference*, Berlin, Germany, Sep. 2007.

[2] Mohammed, A., Mehmood, A., Pavlidou, F.-N., and Mohorcic, M., "The Role of High-Altitude Platforms (HAPs) in the Global Wireless Connectivity," in *Proceedings of the IEEE*, vol. 99, Nov. 2011, pp. 1939–1953. DOI: 10.1109/JPROC.2011.2159690

[3] National Aeronautics and Space Administration, Dryden Flight Research Center, *Solar-Powered Research and Dryden*, NASA Facts: FS-1998-10-0054 DFRC, available online at https://www.nasa.gov/centers/dryden/pdf/120308main_FS-054-DFRC.pdf, 1998.

[4] Teets Jr., E. H., Donogue, C. J., and Wright, P. T., *Meteorological Support of the Helios World Record High Altitude Flight to 96,863 Feet*. Dryden, Flight Research Center, Edwards, California, US: National Aeronautics and Space Administration, May 2002.

[5] D'Oliveira, F., Melo, F., and Devezas, T., "High-Altitude Platforms - Present Situation and Technology Trends," in *Journal of Aerospace Technology and Management*, vol. 8, Aug. 2016, pp. 249–262. DOI: 10.5028/jatm.v8i3.699

[6] Ross, H., "Fly around the World with a Solar Powered Airplane, AIAA-2008-8954," in *The 26th Congress of International Council of the Aeronautical Sciences (ICAS), Anchorage, Alaska*, 2008. DOI: 10.2514/6.2008-8954

[7] Nunez, C., "Solar Impulse 2 Completes Trip Around World, Demonstrates Clean Energy and Aviation," *National Geographic*, 2016, Available online at https://www.nationalgeographic.com/news/2016/07/solar-impulse-completes-trip-around-world-abu-dhabi-solar-power-airplane/.

[8] Malewar, A., "Airbus's solar-powered Zephyr UAS crashes after a 64-day flight," *Inceptive Mind*, Aug. 25, 2022, Available online at https://www.inceptivemind.com/airbus-solar-powered-zephyr-uav-crashes-64-day-flight/25969/ (Accessed: 2025-12-26).

[9] Nikodem, F., "Overview of the DLR High Altitude Platform and Scientific Potential of the Technology Demonstrator HAP-alpha," *Deutscher Luft- und Raumfahrtkongress 2023*, Sep. 2023. [Online]. Available: https://elib.dlr.de/198509/

[10] Weiser, C. and Ossmann, D., "Baseline Flight Control System for High Altitude Long Endurance Aircraft," in *AIAA SciTech Forum 2022*, 2022. DOI: 10.2514/6.2022-1390

[11] Weiser, C., "Verification and Clearance of a Flight Control System for High Altitude Long Endurance Aircraft," in *2025 IEEE Aerospace Conference*, 2025, pp. 1–11. DOI: 10.1109/AERO63441.2025.11068608

[12] Brauchle, J. et al., "MACS-HAP: Design and Image Processing Features of the DLR HAP Camera System," in *IGARSS 2023 - 2023 IEEE International Geoscience and Remote Sensing Symposium*, IEEE, Ed., Pasadena, California, US, Jul. 2023, pp. 4804–4807. DOI: 10.1109/IGARSS52108.2023.10282470

[13] Jirousek, M., Peichl, M., Anger, S., Dill, S., and Engel, M., "Design of a Synthetic Aperture Radar Instrument for a High-Altitude Platform," in *IGARSS 2023 - 2023 IEEE International Geoscience and Remote Sensing Symposium*, IEEE, Ed., Pasadena, California, US, Jul. 2023, pp. 2045–2048. DOI: 10.1109/IGARSS52108.2023.10283363

[14] Hasan, Y. J., Voß, A., Raab, C., and Fezans, N., "HAP-alpha: Development of System Identification Manoeuvres for Low-Altitude Flight Testing of a Flexible High-Altitude Platform," *International Forum on Aeroelasticity and Structural Dynamics*, 2026, submitted.

[15] Hasan, Y. J., Fezans, N., and Voß, A., "Landing Simulation of a High-Altitude Platform with Skid-Type Landing Gear - Flight Procedure, Controller, and Loads," *33rd Congress of the International Council of the Aeronautical Sciences*, Sep. 2022.

[16] Hasan, Y. J. et al., "Flight mechanical analysis of a solar-powered high-altitude platform," *CEAS Aeronautical Journal*, Nov. 2022. DOI: 10.1007/s13272-022-00621-2

[17] Waszak, M. R. and Schmidt, D. K., "Flight Dynamics of Aeroelastic Vehicles," *Journal of Aircraft*, vol. 25, no. 6, pp. 563–571, 1988. DOI: 10.2514/3.45623

[18] Hasan, Y. J., Fezans, N., and Voß, A., "Flight Mechanical Analysis of a Very Flexible High-Altitude Platform Under Uncertainty Considerations," *34th Congress of the International Council of the Aeronautical Sciences*, Sep. 2024.

[19] Hasan, Y. J., Roeser, M. S., and Voigt, A., "Evaluation of the controllability of a remotely piloted high-altitude platform in atmospheric disturbances based on pilot-in-the-loop simulations," *CEAS Aeronautical Journal*, Nov. 2022. DOI: 10.1007/s13272-022-00626-x

[20] Hasan, Y. J., "Evaluation of landing procedures for a high-altitude platform with skid-type landing gear based on pilot-in-the-loop simulations," *CEAS Aeronautical Journal*, Oct. 2024. DOI: 10.1007/s13272-024-00780-4

[21] Schmid, S., Lutz, T., and Krämer, E., "Impact of Modelling Approaches on the Prediction of Ground Effect Aerodynamics," *Engineering Applications of Computational Fluid Mechanics*, vol. 3, no. 3, pp. 419–429, 2009. DOI: 10.1080/19942060.2009.11015280

[22] Lambregts, A. A., "Vertical flight path and speed control autopilot design using total energy principles, AIAA paper 83-2239," in *Guidance and Control Conference, Gatlinburg, Tennessee, USA*, Aug. 1983, pp. 559–569. DOI: https://doi.org/10.2514/6.1983-2239

[23] Lambregts, A. A., "Integrated system design for flight and propulsion control using total energy principles, AIAA paper 83-2561," in *Aircraft Design, Systems and Technology Meeting, Fort Worth, Texas, USA*, Oct. 1983. DOI: https://doi.org/10.2514/6.1983-2561

[24] Lambregts, A. A., "Total Energy Based Flight Control," U.S. Patent 4,536,843, Aug. 20, 1985.

[25] Looye, G., "TECS/THCS-based generic autopilot control laws for aircraft mission simulation," in *Proceedings of the EuroGNC 2013, 2nd CEAS Specialist Conference on Guidance, Navigation & Control*, Delft, The Netherlands, Apr. 2013, pp. 1384–1403. [Online]. Available: https://elib.dlr.de/83741/

[26] Tommasi, M., "Landing Simulations of a Solar-Powered High-Altitude Platform with Skid-Type Landing Gear in the Presence of Lateral Wind Disturbances," DLR-Internal Report DLR-IB-FT-BS-2024-99, M.S. thesis, Politecnico di Torino, 2024. [Online]. Available: https://elib.dlr.de/205046/

[27] Voß, A. et al., "HAP-alpha: Model Updating Based on Ground Vibration Test and the Influence on Loads," *International Forum on Aeroelasticity and Structural Dynamics*, 2026, submitted.